

This is a repository copy of *Hot surface ionic line emission and cold K-inner shell emission from petawatt-laser-irradiated Cu foil targets*.

White Rose Research Online URL for this paper:

<https://eprints.whiterose.ac.uk/id/eprint/65656/>

Version: Published Version

Article:

Theobald, W., Akli, K., Clarke, R. et al. (29 more authors) (2006) Hot surface ionic line emission and cold K-inner shell emission from petawatt-laser-irradiated Cu foil targets. *Physics of Plasmas*. 043102. -. ISSN: 1089-7674

<https://doi.org/10.1063/1.2188912>

Reuse

Items deposited in White Rose Research Online are protected by copyright, with all rights reserved unless indicated otherwise. They may be downloaded and/or printed for private study, or other acts as permitted by national copyright laws. The publisher or other rights holders may allow further reproduction and re-use of the full text version. This is indicated by the licence information on the White Rose Research Online record for the item.

Takedown

If you consider content in White Rose Research Online to be in breach of UK law, please notify us by emailing eprints@whiterose.ac.uk including the URL of the record and the reason for the withdrawal request.

Hot surface ionic line emission and cold K-inner shell emission from petawatt-laser-irradiated Cu foil targets

W. Theobald,¹ K. Akli,³ R. Clarke,⁷ J. A. Delettrez,¹ R. R. Freeman,⁶ S. Glenzer,² J. Green,⁷ G. Gregori,² R. Heathcote,⁷ N. Izumi,² J. A. King,³ J. A. Koch,² J. Kuba,² K. Lancaster,⁷ A. J. MacKinnon,² M. Key,² C. Mileham,¹ J. Myatt,¹ D. Neely,⁷ P. A. Norreys,⁷ H.-S. Park,² J. Pasley,⁵ P. Patel,² S. P. Regan,¹ H. Sawada,¹ R. Shepherd,² R. Snavely,² R. B. Stephens,⁴ C. Stoeckl,¹ M. Storm,¹ B. Zhang,³ and T. C. Sangster¹

¹Laboratory for Laser Energetics, University of Rochester, 250 East River Road, Rochester, New York 14623-1299

²Lawrence Livermore National Laboratory, 7000 East Ave, Livermore, California 94550-9234

³Department of Applied Sciences, University of California, Davis, Davis, California 95616

⁴General Atomics, San Diego, California 92186

⁵University of California, San Diego, California 92093

⁶College of Mathematical and Physical Sciences, Ohio State University, Columbus, Ohio 43210

⁷Rutherford Appleton Laboratory, Chilton, Didcot, Oxfordshire OX11 0QX, United Kingdom

(Received 11 November 2005; accepted 1 March 2006; published online 18 April 2006)

A hot, 2 to 3 keV electron temperature surface plasma was observed in the interaction of a 0.7 ps petawatt laser beam with solid copper-foil targets at intensities $>10^{20}$ W/cm². Copper K-shell spectra were measured in the range of 8 to 9 keV using a single-photon-counting x-ray charged-coupled-device camera. In addition to K_α and K_β inner-shell lines, the emission contained the Cu He $_\alpha$ and Ly $_\alpha$ lines, allowing the temperature to be inferred. These lines have not been observed previously with ultrafast laser pulses. For intensities less than 3×10^{18} W/cm², only the K_α and K_β inner-shell emissions are detected. Measurements of the absolute K_α yield as a function of the laser intensity are in general agreement with a model that includes refluxing and confinement of the suprathermal electrons in the target volume. © 2006 American Institute of Physics.

[DOI: 10.1063/1.2188912]

I. INTRODUCTION

There is much interest in both experimental and theoretical studies of laser-solid target interactions with picosecond laser beams at relativistic intensities because of their relevance to fast ignition in laser fusion¹ and backlighter development.^{2,3} High-intensity, ultrashort laser pulses impinging onto solid or gaseous targets produce large quantities of suprathermal electrons ranging from ~ 100 keV up to several MeV, with conversion efficiencies of several 10% of incident laser energy into electron energy.^{4,2-7} A precise physical understanding of the MeV electron production and transport in dense plasma is crucial for the success of the fast-ignition concept. This has triggered a vigorous research effort in both experimental⁸⁻¹² and theoretical studies.¹³⁻¹⁶

Strong laser self-generated magnetic and electric fields influence the transport of relativistic electrons in high-energy-density plasmas.^{12,15,17} Inhibited heat flux in insulators due to strong longitudinal electrical fields has recently been predicted at subrelativistic intensities with a one-dimensional Monte Carlo collisional particle-in-cell (PIC) code.¹⁸ Depending on the experimental conditions, the fields might collimate the electron beam or compromise the effectiveness of electron penetration because of flux inhibition.^{17,19,20} The guiding of electrons with MeV energy in a plasma fiber over a distance of ~ 1 mm is attributed to strong laser-generated fields.²¹ Many plasma processes influence the heating of solid matter by laser-generated relativistic electrons and their return currents. One example is an

observed annular heating pattern that is attributed to a strong Weibel instability growth because of sharp transverse gradients in the input electron-beam current.¹¹

Hard x-ray bremsstrahlung and characteristic inner-shell line emissions, predominantly from the K shell, are produced when energetic electrons propagate into the bulk of a solid target. The measurement of inner-shell emission lines is a valuable diagnostic to characterize the suprathermal electron distribution.^{4,6,7,22-24} Measurements of electron temperatures and temperature gradients provide important guidance for simulations to study energy transport in relativistic laser-solid density plasmas. The standard method to infer electron density and temperature in laser-produced plasmas is x-ray line spectroscopy;²⁵ this method has been applied to petawatt laser-plasma experiments, e.g., Koch *et al.*, using aluminum K-shell spectra.¹¹ The dense and hot plasma environment shifts and broadens the spectral lines because of the interactions of the charged-particle plasma constituents. The comparison of measured line shapes and line ratios to calculations allows the plasma parameters to be inferred.

In this work, measurements of the surface electron temperatures of petawatt-laser-produced copper plasmas are presented. Measurements of the scaling of the Cu K-shell emission with laser intensity and target thickness are shown and analyzed. The following three sections will present the experimental setup (Sec. II), experimental results (Sec. III), and analysis and discussion (Sec. IV). The fourth section contains two subsections: resonance line emission from hot plas-

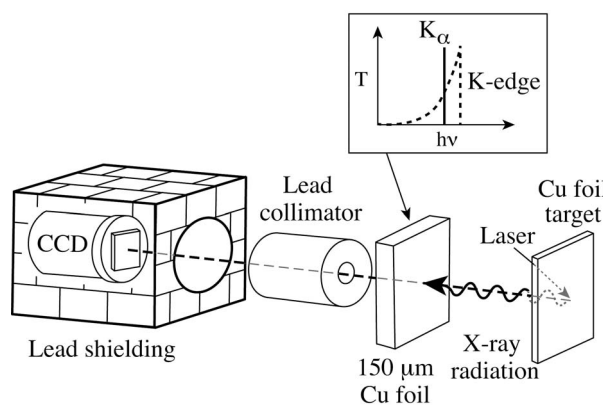


FIG. 1. Experimental setup. The petawatt laser is focused onto a thin copper foil target. A single-hit charged-coupled-device (CCD) camera measures the x-ray emission from the target's front side. Lead collimators and lead shielding provide the necessary suppression of unwanted background radiation. A 150 μm copper foil provides bandpass filtering of the Cu K-shell emission while suppressing the background radiation. The inset shows qualitatively the foil transmission versus photon energy and the position of the K_α line.

mas (Sec. IV A) and inner-shell emission (Sec. IV B) that compares the measured K_α laser-intensity scaling to a model calculation. The summary and conclusions are presented in Sec. V.

II. EXPERIMENTAL SETUP

A schematic of the experimental setup is shown in Fig. 1. Laser pulses from either the Rutherford Appleton Laboratory Petawatt (PW)²⁶ or the 100 TW²⁷ facilities were focused with $f/3$ off-axis parabolas to a spot size of the order of $\sim 10 \mu\text{m}$ in diameter.²⁸ The fraction of the nominal laser energy transported onto the target through the compressor and subsequent optics of the PW and the 100 TW laser systems is 75% and 66%, respectively. About half this energy is contained in the main focal spot while the remainder is distributed over a larger area.^{28,29} The laser energy was measured for each shot before the beam entered the compressor. The maximum achievable intensities on the target were $4(\pm 2) \times 10^{20} \text{ W/cm}^2$ and $4(\pm 2) \times 10^{19} \text{ W/cm}^2$ with the PW and the 100 TW lasers, respectively. The relatively large uncertainty in intensity on target is mainly due to shot-to-shot changes in the focal-spot pattern.

Preplasma formation was measured side-on with a frequency-doubled, 1 ps probe beam and a Wollaston prism interferometer that showed that the plasma surface with an electron density of 10^{19} cm^{-3} expands at most by $40 \mu\text{m}$ from the original target surface at 100 ps prior to the main pulse interaction. Higher electron densities are not accessible by this diagnostic because of probe-light refraction out of the f number of the collecting lens in the probe line. Prepulse measurements show an amplified spontaneous emission (ASE) pulse starting at 1.5 ns ahead of the main pulse with an intensity of 5×10^{-8} of the main pulse intensity. The overall intensity contrast is better than 10^5 in a time window between 10 ns and 50 ps before the main pulse. The p -polarized light was focused at a 30° angle of incidence

onto thin ($< 30 \mu\text{m}$) copper foil targets with an area of $< 2000 \times 2000 \mu\text{m}^2$. The targets were mounted as flags on carbon fibers of $6 \mu\text{m}$ diameter.

A single-photon-counting, x-ray back-illuminated, charge-coupled-device (CCD) camera (SI 800-145, Spectral Instruments-Photonics, Tucson, AZ) measured the plasma emission from the laser irradiation side ("target front side") at a viewing angle of 16° with respect to the target normal. Radiation shielding of the CCD camera with a lead housing and lead collimators was crucial in obtaining good signal-to-noise spectra by suppressing the hard x-ray background generated by the petawatt laser.³⁰ In addition, a 150 μm -thick Cu foil filter in front of the CCD was used to adjust the signal level of the K-shell emission and to improve the signal-to-noise ratio. When an x-ray photon is absorbed in the material of the CCD, a certain number of free-charge carriers proportional to the x-ray photon energy are created, corresponding to 4.56 eV per count for this CCD. The integral fractional number of exposed pixels with energies $> 5 \text{ keV}$ is in the range of 1%–3% and the integrated Cu K-shell emission typically is measured in $\sim 0.3\%$ of the pixels. The percentage of all pixels that register an energy deposition is 25%–50% at $3 \times 10^{20} \text{ W/cm}^2$ and 15%–40% at lower intensities, primarily due to events below 5 keV. These low energy hits might be generated by a fractional deposition from high energy x rays and fluorescence radiation from the inside of the CCD chamber walls. Within this low level of Cu K-shell emission pixel exposure, the CCD is operating in a single-photon-counting mode.³¹ The experimental setup with the 100 TW facility was similar to that described previously. The CCD detector was located closer to the plasma source in that case, 1.4 m instead of 3.8 m, leading to an increased solid angle by a factor of ~ 7 .

A significant number of x-ray events are split between adjacent pixels. Adding the value of the pixels surrounding the event centroid might be used to reconstruct the total charge collected from an event. This is useful at very low photon fluxes, especially in astronomical applications. The single pixel analysis used here ignores the spread of the absorbed x-ray energy over several pixels and typically takes only $\sim 20\%$ of the absorbed 8 to 9 keV photons into account.³¹ Single pixel analysis has a slightly higher spectral resolution than summed pixel analysis.^{31,32} It is also less sensitive to the higher background observed in PW laser-plasma interaction experiments. A CCD quantum efficiency of $\sim 10\%$ with a single pixel analysis is reported in the 8 to 9 keV range for an x-ray imaging spectrometer used in the x-ray astronomical satellite Astro-E.³¹ A quantum-efficiency measurement of an SI-800 camera at 8 keV revealed a value of $\sim 5\%$ with single-pixel analysis.³³ The same kind of chip (CCD42-40 chip, e2v technologies, Chelmsford UK) was used in the two SI cameras: one for calibration and one in this experiment. The quantum efficiency is a factor of 2 lower compared to the Astro-E CCD, which is probably due to the smaller pixel size and a thinner depletion layer of the SI-800 chip.

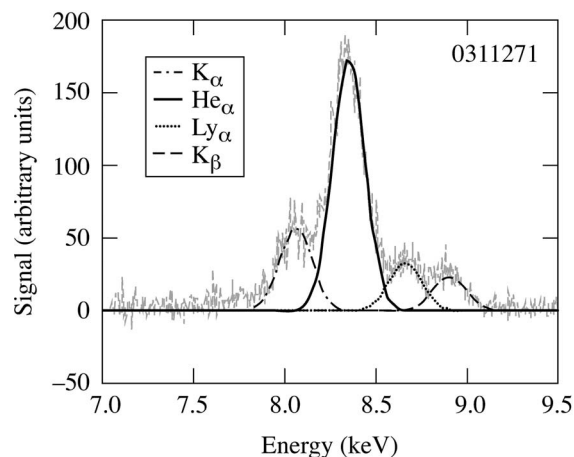


FIG. 2. Copper K-shell spectrum from the target's front side for a laser intensity of 3×10^{20} W/cm² and a pulse duration of 0.7 ps and $E_L = 447$ J. The gray curve denotes the measurement while the other curves are Gaussian fits to the various emission lines. The He α resonance line of helium-like copper ion dominates the spectrum.

III. EXPERIMENTAL RESULTS

Figure 2 shows a copper K-shell spectrum from the target's front side for laser shot 0 311 271. A laser pulse with energy of 447 J and a pulse duration ~ 0.7 ps was focused to an intensity of $\sim 3 \times 10^{20}$ W/cm² onto a 20 μ m-thick Cu foil target. The continuum x-ray background is subtracted while the filter transmission of the 150 μ m Cu foil has not yet been taken into account. The measured spectrum (gray curve) consists of four overlapping lines. The other curves denote a fit of Gaussian line shapes to the measurement, indicating a full-width at half-maximum (FWHM) of ~ 220 eV for each line. The four peaks are identified as the lines of the Cu K α (8.05 keV), He α (8.35 keV), Ly α (8.69 keV), and K β (8.91 keV) transitions.^{34,35} The He α line dominates the spectrum. The observation of He α and Ly α is distinctly different from Cu K-shell spectra observed previously with ultrashort laser pulses at lower laser intensities.²⁴ The appearance and intensity of the He α and Ly α lines depend strongly on the laser intensity, as shown in Fig. 3. The K-shell emission was measured with 0.7 ps pulses for various laser intensities between $\sim 2 \times 10^{18}$ W/cm² and $\sim 3 \times 10^{20}$ W/cm² by varying the spot size within 10 to 100 μ m and the beam energy in the range from ~ 200 to ~ 500 J. The Ly α line of hydrogen-like copper disappears below 3×10^{20} W/cm², while He α is observed down to 1×10^{19} W/cm², and only K α and K β are measured at 2.5×10^{18} W/cm². No measurements with 0.7 ps pulses are available between 2.5×10^{18} W/cm² and 1×10^{19} W/cm². Additional measurements in this intensity range with longer pulses (5 to 14 ps) show the He α signal down to $\sim 6 \times 10^{17}$ W/cm². For 0.7 ps pulses, the noise level prevents the detection of He α below 3×10^{18} W/cm², while for higher intensities it is always measured and steadily increases with laser intensity. In contrast, K α and K β stay about constant between 2×10^{18} W/cm² and 1×10^{20} W/cm² and slightly decrease for intensities above 10^{20} W/cm².

The absolute number of x-ray photons in each line normalized to the laser energy contained in the central laser spot

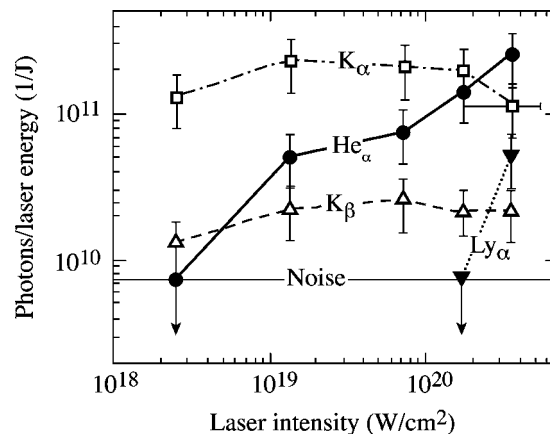


FIG. 3. Integral x-ray photon number normalized to the laser energy contained in the central laser spot as a function of the laser intensity for Cu K α (open squares), He α (solid dots), K β (open triangles), and Ly α (solid triangles). Square Cu foils with thicknesses of 20 μ m and 30 μ m and areas ranging from $500 \times 500 \mu\text{m}^2$ through $2000 \times 2000 \mu\text{m}^2$ were used. The intensity was varied by the focal spot (10 to 100 μ m) and the beam energy (~ 200 to ~ 500 J) while keeping the pulse duration constant at 0.7 ps. The apparent threshold of Ly α is 3×10^{20} W/cm², while only K α and K β are observed at 2.5×10^{18} W/cm². A representative error bar of the laser intensity is shown for one K α data point.

was calculated by integrating the number of hits and by taking the solid angle, filter transmission, and quantum efficiency of the CCD in single-pixel analysis mode into account. An isotropic emission into a 4π steradians solid angle is assumed. Reabsorption of the radiation inside the foil target has not been taken into account. The total amount of CCD image exposure influences the calculation of the line yield since pixels that absorb, e.g., a K α photon and a low energy photon will be upshifted in the histogram. This contribution merges in the background and is subtracted from the spectrum. All photon numbers were corrected for this effect by determining the fractional chip exposure x for each CCD image. The line emission yields were then multiplied by a factor of $f = 1/x/(1-x)$, which is on average ~ 1.5 . This is justified since the histogram below 5 keV contributed to more than 97% of all exposed pixels. The relative error bars are estimated to be $\sim 40\%$, based on the standard deviation of several measurements at the same intensity, and the error of f . The absolute uncertainty is estimated to be a factor of 2.4 based on an estimated uncertainty in the CCD quantum efficiency for single-pixel analysis and the relative measurement error.

The Cu K-shell spectrum was studied as a function of the foil thickness with the 100 TW laser facility for low-mass, small-area targets. Figure 4 shows the measured K α , He α , and K β lines for Cu foils of various thicknesses. Laser pulses with 14 ps (a) and 10 ps [(b)–(d)] durations and beam energies of ~ 100 J were focused to an $\sim 10 \mu$ m spot size, providing an intensity of $\sim 3 \times 10^{18}$ W/cm². The thickness is indicated in each figure. The foil area was $500 \times 500 \mu\text{m}^2$ in (a) while it was $100 \times 100 \mu\text{m}^2$ in (b), (c), and (d). The ratio of K α to He α emission changes with thickness, and the relative helium-like emission, becomes larger with thinner foils for the smaller areas. Only a limited number of spectra were sampled, however, and shot-to-shot fluctuations

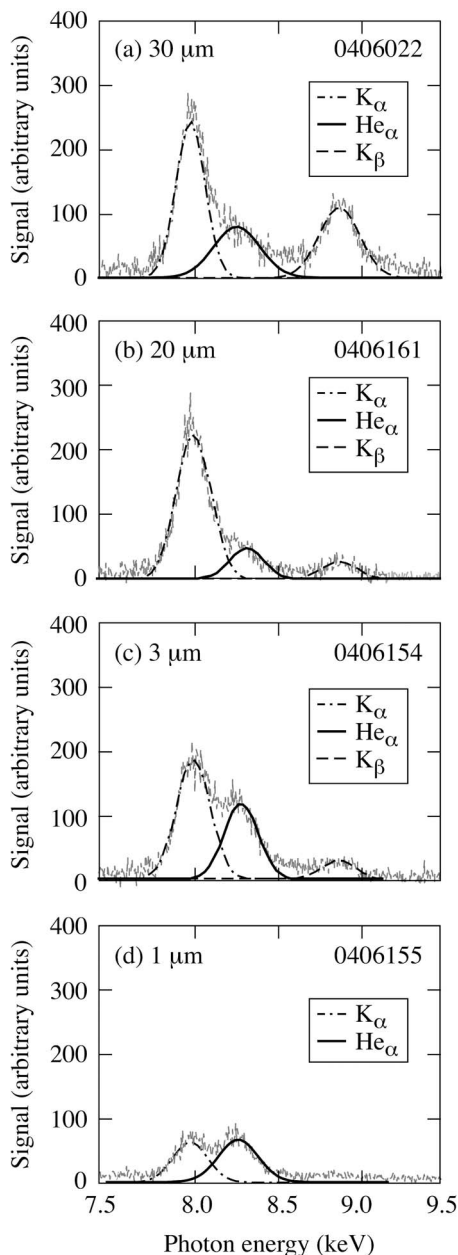


FIG. 4. K-shell spectra showing the K_{α} , He_{α} , and K_{β} lines for various Cu foil thicknesses, as is indicated in each figure. The foil areas were $500 \times 500 \mu\text{m}^2$ (a) and $100 \times 100 \mu\text{m}^2$ for the measurements in (b)–(d). The laser energies in (a)–(d) were 102 J, 118 J, 116 J, and 97 J, respectively. Laser pulses with 14 ps (a) and 10 ps (b)–(d) durations were focused to an $\sim 10 \mu\text{m}$ spot, providing intensities of $\sim 3 \times 10^{18} \text{ W/cm}^2$.

particularly influence the He_{α} signal. The resulting x-ray photon number per laser energy is plotted semilogarithmically as a function of the foil thickness in Fig. 5. The cold inner-shell emission that is created mainly by suprathermal electrons traversing the foil behaves differently than the ionic line emission. The K_{α} signal is relatively independent of foil thickness. A significant decrease is observed only below $3 \mu\text{m}$, which might be due to several effects: (1) an increased volumetric heating might lead to a depletion of cold material, and (2) an increased transfer of hot-electron energy into channels other than K_{α} emission for very low volume targets, notably ion acceleration,^{36,37} might quench the inner-

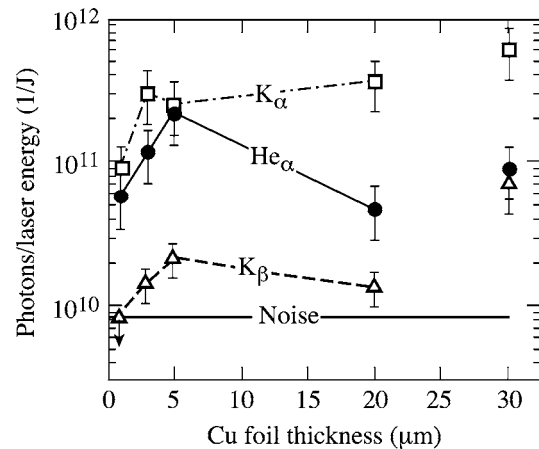


FIG. 5. X-ray photon number per laser energy in the central laser spot versus foil thickness determined from the measured cold K_{α} , K_{β} , and the hot He_{α} emission. The experimental conditions are the same as in Fig. 4. The foil volume diminished from 30 to $20 \mu\text{m}$ by a factor of ~ 40 because of the smaller area. An increased volume heating probably depletes the copper M-shell population, yielding a decreased K_{β} signal while the K_{α} is not significantly affected.

shell signal. The K_{β} intensity drops by a factor of ~ 5 from 30 to $20 \mu\text{m}$, and then stays about constant with smaller thicknesses and decreases again below $3 \mu\text{m}$. The strong decrease from 30 to $20 \mu\text{m}$ is probably due to the larger foil area, which is further discussed in Sec. IV A. While the inner-shell x-ray photon number decreases with thinner foils, the ionic line emission seems to show an opposite trend for large thicknesses. The He_{α} signal first increases with diminishing thickness, peaks at $5 \mu\text{m}$, and then decreases to its initial value at $1 \mu\text{m}$. The relatively large scattering of the values is probably due to shot-to-shot fluctuations in the laser conditions and the focus position on the small target.

Evidence that the ionic emission originates from front-surface plasmas was obtained from measurements of Cu-foil targets covered with a thin layer of a different material. Figures 6(a)–6(c) show spectra at an intensity of $1.5 \times 10^{20} \text{ W/cm}^2$ on copper-foil targets without a cover layer [Fig. 6(a)], with a $1 \mu\text{m}$ -thick aluminum layer [Fig. 6(b)], and with a $0.5 \mu\text{m}$ -thick tantalum layer [Fig. 6(c)]. The comparison of Figs. 6(a) and 6(b) shows that the He_{α} emission is reduced by a factor of ~ 5 , while K_{α} and K_{β} are diminished by a factor of ~ 2 . The data suggest that, with the Al coating, the hot plasma is created mainly in the aluminum with relatively little heating of the copper. The reduction in K_{α} and K_{β} may indicate the stopping of hot electrons in the Al layer. The Ly_{α} is not observed at this laser intensity. An additional experiment, Fig. 6(c), at the same intensity with a $0.5 \mu\text{m}$ Ta overcoat on $20 \mu\text{m}$ Cu foil gives further evidence that the Cu He_{α} line emission originates from a thin layer on the target's front side. Besides the Cu K_{α} and a strong L-shell emission from tantalum peaking at 8.75 keV , no Cu He_{α} line at 8.35 keV is measured. The mass densities of solid tantalum and aluminum are 16.7 g/cm^3 and 2.7 g/cm^3 , respectively. The factor of 6 higher mass density explains why Ta is more efficient in blocking energy transport through the surface despite half of the film thickness, leading to plasma tempera-

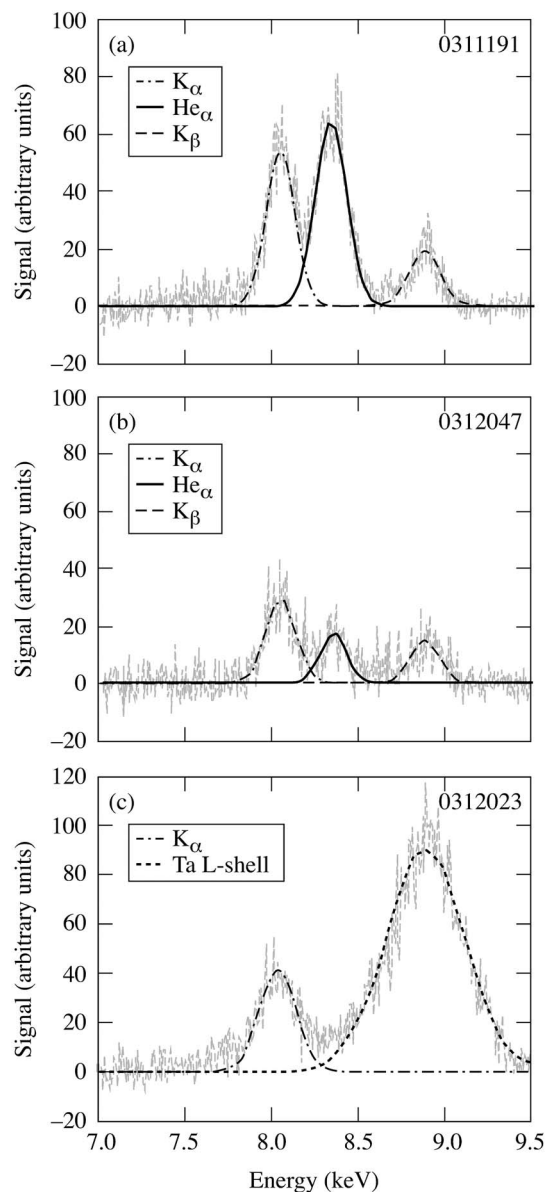


FIG. 6. Copper K-shell spectra with the target's front side covered with a thin layer of different materials that leads to a suppression of the ionic line emission. (a) is without a cover layer, while (b) and (c) denote the results with a $1\text{ }\mu\text{m}$ -thick aluminum and with a $0.5\text{ }\mu\text{m}$ -thick tantalum layer, respectively. The He_α line emission is strongly reduced (b) and even absent (c) compared to the no cover layer (a), indicating that the hot plasma is generated in a thin layer on the target's front side. The laser energies, pulse duration, and intensity were 254 J (a), 227 J (b), 227 J (c), 0.7 ps, and $\sim 1.5 \times 10^{20}\text{ W/cm}^2$.

ture at the Ta-Cu boundary that is not sufficient to generate He-like Cu ions.

It is interesting to compare the result from copper ($Z=29$) to the K-shell emission of a target material with a much higher atomic number. Figure 7 shows the result of an experiment with a $50\text{ }\mu\text{m}$ -thick silver foil target ($Z=47$) at $\sim 2 \times 10^{20}\text{ W/cm}^2$. Only the inner-shell emission (but no He_α and Ly_α lines) is observed for the higher- Z target. This indicates that the temperature is not high enough to create He- and H-like silver ions, which require estimated electron temperatures above $\sim 50\text{ keV}$.³⁸

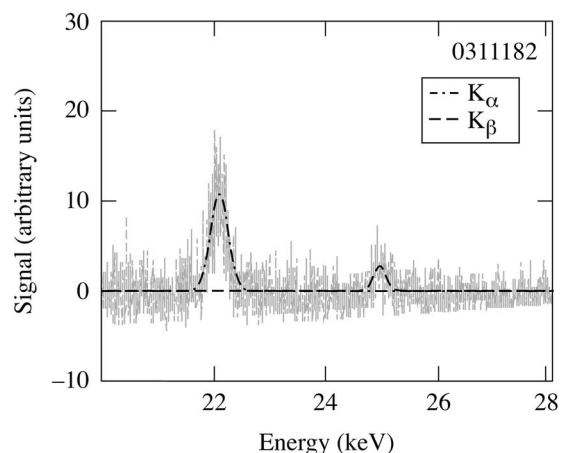


FIG. 7. Measurement of the silver K-shell emission from a $50\text{ }\mu\text{m}$ -thick Ag-foil target. The laser energy, pulse duration, and intensity were 275 J, 0.7 ps, and $\sim 2 \times 10^{20}\text{ W/cm}^2$, respectively. Only K_α and K_β inner-shell emission lines are measured, but no ionic line emission.

IV. ANALYSIS AND DISCUSSION

Two emission processes occur in these experiments: inner-shell emission and ionic resonance-line emission. The K_α and K_β lines are emitted by inner-shell transitions when an L- or M-shell electron fills a vacancy in the K shell, and the corresponding excess energy is radiated away by a photon in competition with Auger decay. X rays and energetic electrons may both produce inner-shell vacancies, assuming that the radiation has sufficient energy to excite above the K edge (for Cu $h\nu > 9\text{ keV}$). Indirect inner-shell emission due to the absorption of continuous x-ray radiation that is produced while suprathermal electrons decelerate in the target is, however, relatively negligible for elements with an atomic number < 30 .³⁹ Energetic electrons are the main contribution to K_α and K_β production in a high-intensity, ultrashort, laser-solid interaction with low- and mid- Z materials.^{22,24} In contrast, the He_α and Ly_α lines are electronic transitions from the first excited to the ground level in the helium-like and hydrogen-like ions. Sufficient thermal plasma temperatures are required to generate these highly stripped ions. While the inner-shell radiation originates from the cold bulk material, the ionic lines are produced in hot plasmas on the laser target sides, as shown in a schematic in Fig. 8.

A. Resonance-line emission from hot plasmas

Calculations with the commercially available *PrismSPECT* program⁴⁰ were performed to estimate the plasma conditions that lead to the ionic resonance-line emission from the hot plasma. *PrismSPECT* is a collisional-radiative code that takes the details of the excitation and deexcitation paths, opacity, and atomic physics into account. The plasmas are assumed to be in steady state, non local thermodynamic equilibrium conditions in slab geometry with a specified thickness, and have a homogeneous density and electron temperature. Time-dependent collisional-radiative calculations of the ionization dynamics of solid-density aluminum plasmas at electron temperature $T_e = 1\text{ keV}$ show that steady-state conditions are established within $\sim 0.5\text{ ps}$.⁴¹ Similar

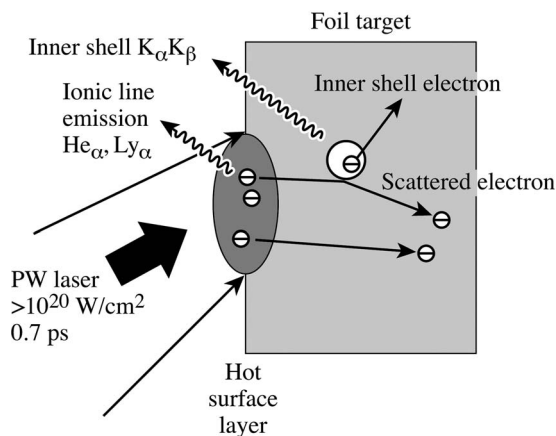


FIG. 8. Schematic representation of the ionic line and inner-shell emission generation process. The ionic lines stem from a hot surface layer while fast electrons produce the inner-shell emission.

time-dependent calculations performed for $T_e = 1$ keV and $n_e = 10^{23} \text{ cm}^{-3}$ show that Cu plasmas are reaching steady state within ~ 1 ps.⁴² Steady state is therefore a reasonable assumption for near-solid-density plasmas in our experiment. Suprathermal electrons were not included in the calculation. This assumption is supported by calculations of the charge-state distribution of a 1 keV, 10^{23} cm^{-3} Cu plasma, including the ionization effect of a hot-electron component. The charge-state distribution is essentially given by the thermal plasma, and up to a fraction of 10% of hot electrons with an average energy of 3 MeV has no significant influence.⁴² The overcoat measurements (Fig. 6) show that the hot plasma is formed from a layer that has initially $t \approx 1 \mu\text{m}$ thickness at solid density. Figure 9(a) shows a comparison for shot 0 311 271 (solid square symbols) to calculations for an electron density of $n_e = 2.3 \times 10^{24} \text{ cm}^{-3}$, $t = 1 \mu\text{m}$, and various electron temperatures between 1 and 3 keV. The electron density corresponds to a solid density of $n_{\text{ion}} = 8.5 \times 10^{22} \text{ cm}^{-3}$ and an average degree of ionization of 27. The K_α and K_β lines are suppressed to allow a better comparison of the resonance-line emission to the calculations. The filter transmission of the 150- μm Cu foil was taken into account, and the calculated spectra were convolved with an instrumental resolution of 200 eV. The *PrismSPECT* calculation reveals that the measured He_α peak is a complicated array of lines, including the He_α line, the intercombination line, dipole forbidden lines, and lithium-like ion satellite lines that merge together. The effective linewidth of this feature is ~ 90 eV at solid density and explains the slightly larger measured spectral FWHM of ~ 220 eV for He_α . The ratio of He_α and Ly_α is sensitive to the temperature and a good agreement is obtained for $T_e = 1.8$ keV.

The ASE laser pulse pedestal causes some ablation of the front layer before the main laser pulse impinges on the target. The main pulse then interacts with less than solid density plasma and an increased density scale length. The density profile depends on the laser contrast, pulse profile, and hydrodynamic expansion of the preplasma. To model the density profile generated by the ASE pulse, a two-

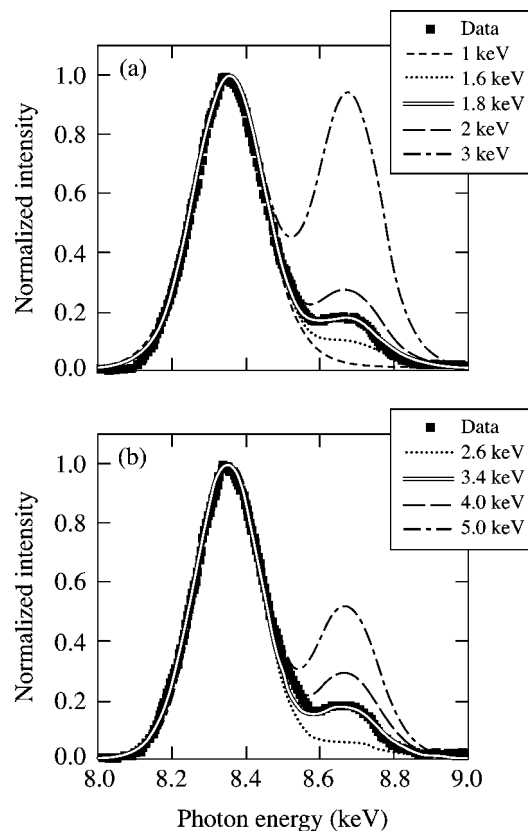


FIG. 9. A comparison of the experimentally measured ionic resonance line emission (solid square symbols) to calculations with the computer program *PrismSPECT*⁴⁰ for (a) solid-density ($n_e \approx 2.3 \times 10^{24} \text{ cm}^{-3}$) $1 \mu\text{m}$ thick plasma slab and various electron temperatures between 1 keV and 3 keV. (b) shows a comparison for an electron density of $2.3 \times 10^{23} \text{ cm}^{-3}$, plasma slab thickness of $1 \mu\text{m}$, and various electron temperatures between 2.6 keV and 5 keV.

dimensional hydrodynamic simulation of the expansion and structure of the preplasma was performed using the Eulerian code *POLLUX*.⁴³ A $2.5 \times 10^{13} \text{ W/cm}^2$ Gaussian temporal pulse shape with a 1.5 ns pulse duration was assumed. In the radial direction, a Gaussian-shaped intensity profile with a FWHM of $7 \mu\text{m}$ was used for the simulation. Figure 10 shows a lineout of the calculated electron-density profile

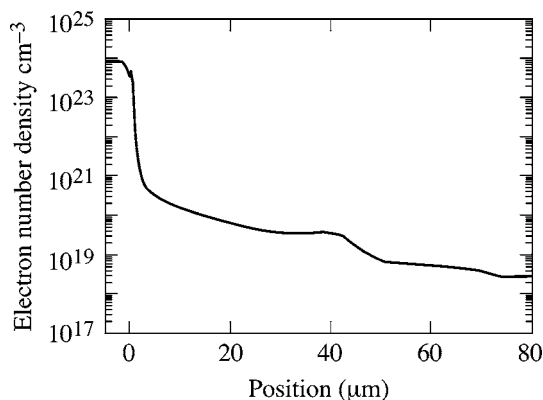


FIG. 10. Calculated electron density profile along the target normal that is generated by an ASE prepulse; see the text for details. The 2-D Eulerian code *POLLUX*⁴³ was used for the simulation.

along the target normal at the peak of the interaction pulse. The critical density has expanded $\sim 2 \mu\text{m}$ from the original surface. The interaction of the main pulse with relativistic intensities and the corresponding electron mass increase leads to a higher critical density than in the nonrelativistic case. A distance of $\sim 1 \mu\text{m}$ is then calculated for the relativistic corrected critical density. The distance from the original target surface to the 10^{19} cm^{-3} contour is $\sim 45 \mu\text{m}$, which agrees well with the shadowgraph measurements. Preplasma formation on the Vulcan 100-TW laser has been previously experimentally and theoretically investigated.^{37,44} Density scale lengths of $\sim 3 \mu\text{m}$ and $\sim 10 \mu\text{m}$ were determined at the critical density and at one-tenth of the critical density, respectively.

The density profile shows that the ablated mass below critical density is a factor of ~ 10 smaller compared to the $1 \mu\text{m}$ layer from critical density up to solid density. Accordingly, the number of ionic line emitters in the ablation plume is negligible compared to the emitter number above the critical density, where most of the absorbed laser energy is deposited. The thermal energy transport distance into the target is estimated to be several microns at close to solid density based on the overcoating experiments. Figure 9(b) shows a comparison of measured and calculated spectra for $n_e = 2.3 \times 10^{23} \text{ cm}^{-3}$, $t = 1 \mu\text{m}$, and various temperatures, with the best agreement at $T_e = 3.4 \text{ keV}$. Not shown is the comparison for $n_e = 2.3 \times 10^{23} \text{ cm}^{-3}$ and $t = 10 \mu\text{m}$, yielding $T_e = 2.6 \text{ keV}$, which has roughly the same emitter number as the solid density, $t = 1 \mu\text{m}$ calculation. Opacity effects in the blowoff plasma are negligible because of the low concentration of He- and H-like ions. The electron temperature is thus estimated to be in the range of 2 to 3 keV for a close to solid density plasma and a slab thickness between 1 and $10 \mu\text{m}$. The number is in agreement with highly resolved Cu K-shell spectral measurements performed at similar experimental conditions, yielding a front side electron temperature of $\sim 2 \text{ keV}$.⁴⁵

Two-dimensional opacity effects and heating of the underdense plasma by the short interaction pulse were not considered. Optical-field-ionized He- and H-like ion generation in the underdense plasma along the laser channel is negligible. Using a simple over-the-barrier suppression calculation for electric field ionization,⁴⁶ estimated saturation intensities of $2 \times 10^{20} \text{ W/cm}^2$ and $7 \times 10^{22} \text{ W/cm}^2$ are required to produce helium- and hydrogen-like copper ions with an ionization probability close to unity. The creation of He-like Cu ions by field ionization is therefore possible only at the highest accessible laser intensity. Ponderomotively accelerated electrons and ions in a radial direction³⁷ that might modify the charge-state distribution of the plasma as well as the velocity gradients because of the tight-focusing condition and the resulting spherical expansion geometry that might affect the opacity⁴⁷ were not included in the analysis.

A precise comparison between the measured absolute He_α and Ly_α photon numbers and the predicted numbers by *PrismSPECT* are not straightforward and out of the scope of this paper. A detailed knowledge of the angular emission characteristic, source area, and temporal emission characteristic is required. Laser plasmas are highly transient with

strong spatial gradients in density and temperature, and a comparison to the measurement requires detailed multidimensional hydrodynamic simulations coupled to a multidimensional, time-dependent radiation transport model. An estimate of the source area may be obtained from measurements of Cu K_α images, typically yielding an area of 50 to $100 \mu\text{m}$ FWHM in diameter,^{12,24} and from Ni Ly_α imaging measurements with $\sim 30 \mu\text{m}$ spots that were obtained under similar experimental conditions.⁴⁵ Town *et al.*, recently reported on simulations to calculate K_α images for comparable experimental conditions and obtained good agreement with measured K_α spot sizes.⁴⁸ Assuming an isotropic He_α and Ly_α emission and neglecting multidimensional and time-dependent opacity effects, the comparison of measured photon numbers and steady-state calculations for a solid-density, $t = 1 \mu\text{m}$ surface layer plasma suggests average emission times of several picoseconds.

The increase in He_α emission with laser intensity above 10^{18} W/cm^2 (Fig. 3) shows an increasing temperature with intensity in the solid-density plasma where electron-ion collisions create the ions in the hot-plasma environment. This might be due to the increasing energy deposition per unit area with higher laser intensities or due to an enhanced energy transport into the solid resulting in higher temperatures and a larger fraction of He- and H-like Cu ions. The absorption of the laser energy takes place in the density range close to the critical density and is dominated by collisionless absorption mechanisms that produce electrons with quasi-Maxwellian energy spectra and temperatures from hundreds of keV to several MeV for the intensities discussed here.⁴⁹ The angular distribution is generally into the target. The electron source parameters vary with the local intensity and therefore also have a spatial pattern related to the laser focal-spot intensity pattern. Energy transport by these electrons is highly complicated and not fully understood. Their binary collision range is generally much greater than the thin layer, which is strongly heated. Several processes may contribute to localizing energy deposition in a surface layer. An Ohmic potential due to the cold electron return current can limit electron penetration, as discussed by Bell *et al.*¹⁹ Electrons can be trapped at the surface by their small Larmor radius in the surface region azimuthal thermoelectric B field generated by the axial increase of density and radial decrease of temperature (dB/dt scaling as $\nabla N \times \nabla T$), with the axial ambipolar electric field in the blowoff plasma causing a rapid radial drift (scaling as $E \times B$). This effect, well known from nanosecond experiments, particularly with CO_2 lasers, has been discussed in connection with petawatt-class, short-pulse experiments by Stephens *et al.*¹² and modeled recently by Mason *et al.*⁵⁰ Three-dimensional PIC simulations by Sentoku *et al.*,¹⁶ have shown that there can be very strong collisionless energy deposition in a thin surface layer attributable to the "Ohmic" heating effect of the return current due to anomalous resistivity induced by the scattering of the return current electrons on microscopic clumps of the B field generated by collisionless Weibel and two-stream instability.

The energy required to create a significant amount of He-like and H-like Cu ions is estimated by assuming the mass of the hot layer to be equivalent to a $\sim 1 \mu\text{m}$ -thick

layer at solid density, as determined from the overcoat experiments. For example, an energy of ~ 3.5 J is needed to heat a mass of solid copper contained in a disk with a $50\text{ }\mu\text{m}$ diam and $1\text{ }\mu\text{m}$ thickness to ~ 3 keV and the resulting average charge state of 27. This is small compared to laser energies of the order of 100 J.

It should be noted that the spectral measurements indicate that K_α and He_α are two distinctive lines with no significant continuum merged between them. This is supported by highly resolved measurements with a crystal spectrograph under similar experimental conditions.⁵¹ The upshift of K_α emission from partially ionized Cu ions has been discussed by Gregori *et al.*⁵¹ There is a small spectral shift as M-shell electrons are removed because of the heating of the bulk of the target by binary collisions of hot electrons and Ohmic heating by the return current. It is indistinguishable in our low-resolution K_α spectra. The removal of L-shell electrons at higher temperatures gives larger shifts as the hot layer is heated and emission occurs at each stage of ionization. The He-like ion is, however, present over a wide temperature range and, in particular, during the emission occurring after the initial heating, leading to a dominant He_α spectral feature in our spectra. This heating partially ionizes the bulk, resulting in a K_α emission shifted to higher energies.

Measurements of the K-shell emission as a function of foil thickness between 30 and $1\text{ }\mu\text{m}$ for a constant laser intensity of $\sim 3 \times 10^{18}\text{ W/cm}^2$ show that the K_α emission remains about constant, with diminishing foil thicknesses down to $3\text{ }\mu\text{m}$. This is expected if no other hot-electron energy-loss mechanisms become significant; the electron temperature of the foil is so low that ionization does not significantly affect the L shell, and the majority of the electrons are refluxing from an electrostatic sheath field. The decreasing yield for targets thinner than $3\text{ }\mu\text{m}$ may imply that a significant amount of cold material is depleted. Another possible explanation is that for very small volume targets, additional energy dissipation channels draining hot-electron energy may become important and influence the K_α signal. A possible channel is energy transfer into accelerated ions that is enhanced in very thin targets.³⁶ The K_β yield is expected to be more sensitive to a temperature increase of the bulk of the target since K_β is eliminated when the M shell is ionized, which might explain the decrease by factor of ~ 5 from 30 to $20\text{ }\mu\text{m}$ while no change is measured for K_α . The target volume changed by a factor of ~ 40 because a $500 \times 500\text{ }\mu\text{m}^2$ foil area was used at $30\text{ }\mu\text{m}$ thickness while $100 \times 100\text{ }\mu\text{m}^2$ was applied for the thinner targets. Recently, similar observations were reported and it was discussed how the laser heating of very small target volumes affects the inner-shell emission.⁵² The resonance-line emission from the $1\text{ }\mu\text{m}$ top layer is not expected to be significantly affected by the foil thickness. Nevertheless, a varying He_α emission is observed with a peak at $5\text{ }\mu\text{m}$ thickness. This variability may be due to slight changes in the laser conditions from shot to shot. As shown in the measurement in Fig. 3, the He_α signal is more sensitive to the applied laser intensity than the inner-shell emission.

B. Inner-shell emission

The measured K_α photon numbers, per unit laser energy, are in general agreement with other experiments.^{20,24} In Ref. 20, $2 \times 10^{11}/\text{J}$ K_α photons were reported for $8\text{ }\mu\text{m}$ -thick Cu foil targets irradiated with 528 nm laser pulses at intensities of $\sim 10^{19}\text{ W/cm}^2$. Similar numbers were reported in Ref. 24, however, those experiments used thick targets where the re-absorption of the K_α photons was strong, and the controlling mechanism was the interplay between the electron-penetration depth relative to the K_α photon-attenuation length. With the targets considered here, reabsorption gives a modest correction; e.g., for solid copper, the transmission fraction f_{trans} is estimated to be 0.91, 0.69, and 0.58 for foil thicknesses of $d=5, 20$, and $30\text{ }\mu\text{m}$, respectively.

The expected number of photons generated, N_k , can be computed by integrating along the path of electrons whose initial energies are described by an energy distribution $f(E_0)$ as long as the electron stays within the material; its energy loss is accurately described with a continuous slowing down formula (dE/ds), and that cold cross sections σ_k for K-shell ionization are appropriate (note that for copper, only direct K-shell ionization is significant³⁹). The yield N_k is then given by

$$N_k = N_e \int_0^\infty dE_0 f(E_0) \int_{E_0}^0 dE \omega_k n_{\text{Cu}} \sigma_k \left(\frac{dE}{ds} \right)^{-1}, \quad (1)$$

$$= N_e \int_0^\infty dE_0 f(E_0) \int_0^{s(E_0)} ds \omega_k n_{\text{Cu}} \sigma_k, \quad (2)$$

where N_e is the total number of hot electrons, $\omega_k=0.425$ is the fluorescence yield, and n_{Cu} is the number density of copper atoms in the target. From this model the electron-to- K_α photon-generation efficiency $\eta_{e \rightarrow k}$ can be determined. This efficiency is defined as $E_k = \eta_{e \rightarrow k} E_e$, where the energy in the electrons is given by $E_e = N_e \int E f(E) dE$ and in K_α photons by $E_k = \varepsilon_k N_k$ with ε_k being the fluorescence energy (8.05 keV for copper K_α). This simple model accounts only for the collisional energy loss and neglects other energy loss effects like, e.g., Ohmic effects and fast ions.

A direct comparison between the experimental production efficiency (yield/laser energy) and the calculated generation efficiency is not straightforward. The experimentally observable quantity is the measured total number of K_α photons, $N_{k,\text{obs}}$, from which the efficiency may be computed as

$$\eta_{e \rightarrow k} = \frac{\varepsilon_k (N_{k,\text{obs}}/f_{\text{trans}})}{E_L} \frac{1}{\eta_{L \rightarrow e}} \quad (3)$$

only if the transmission fraction and the hot-electron production efficiency $\eta_{L \rightarrow e} = E_e/E_L$ are known. Here, E_L is the energy in the laser pulse. The transmission fraction can be easily computed, but the electron-production efficiency is uncertain. Assuming that the hot-electron density within the foil is uniform, the K_α photon transmission fraction is estimated by $f_{\text{trans}} = (L_a/d)[1 - \exp(-d/L_a)]$ with the attenuation length $L_a = 25\text{ }\mu\text{m}$ for K_α . The predicted efficiency, obtained

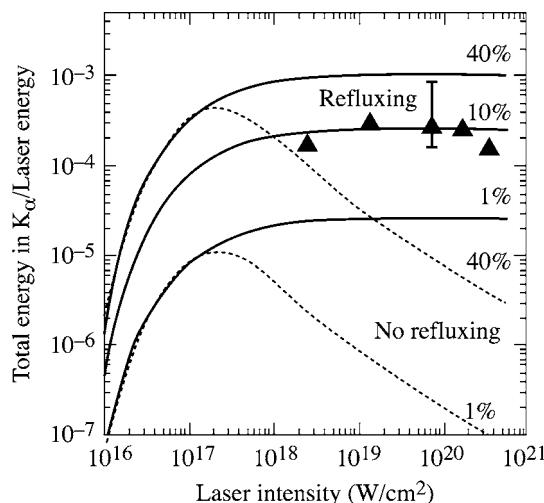


FIG. 11. Total energy in K_α photons normalized to laser energy in the central laser spot as a function of laser intensity. The solid triangles are the experimental data points. The solid curves correspond to the model described in Sec. IV B with perfect confinement of the hot electrons (refluxing) and with a hot electron conversion efficiency of 40%, 10%, and 1%. The dashed curves correspond to the case (40% and 1%) with no refluxing, as described in the text. A representative error bar shows the estimated efficiency uncertainty of the measurement.

using Eq. (1), further requires specification of the hot-electron spectrum $f(E)$.

The predicted total K_α energy of the model divided by the laser energy, together with experimental data, are shown in Fig. 11 for different $\eta_{L \rightarrow e}$ assuming exponentially distributed electron energies, $f(E)dE = (1/T)\exp(-E/T)dE$, and using slowing down and cross section data from the ITS code.⁵³ The total K-shell ionization cross section is from Ref. 54 and, unlike the cross section in Ref. 39, it is valid for relativistic electron energies. For highly relativistic electrons, the cross section increases with particle energy. In Ref. 55, an increased K_α yield was measured with laser intensities above 10^{19} W/cm² and attributed to the growing K-shell ionization cross section with electron energy for relativistic electrons. In contrast to this work, an increase in the K_α yield with the laser intensity is not observed. Calculations have also been performed with a three-dimensional (3-D) relativistic distribution function, leading to slightly higher predicted K_α conversion efficiencies, but with no change to our overall conclusions. Although different intensity temperature scaling appears in the literature,^{29,56} in Fig. 11 we have chosen the ponderomotive scaling of Wilks,^{13,57} $T_{\text{MeV}} = 0.511 [(1 + I_{18} \lambda_{\mu\text{m}}^2 / 1.37)^{1/2} - 1]$, to connect the laser intensity to the hot-electron temperature. No spatial-laser intensity distribution was taken into account in this calculation.

In Fig. 11, the experimental data is almost independent of laser intensity, except at the highest laser intensity, $I = \sim 3 \times 10^{20}$ W/cm². This independence of efficiency on hot-electron temperature, over the experimental range of intensities, is a consequence of Eq. (1), as displayed by the solid model curves. The efficiency is determined by the relative importance of energy loss due to nonionizing collisions and the cross section for K-shell ionization. The latter is quite flat for energies above 100 keV,⁵⁸ while the collisional

cross section drops with increasing energy. The electron range is not restricted by the target thickness for the solid curve in order to mimic the effect of electron refluxing. The net result is that the number of photons produced per unit electron energy is only a weakly increasing function of intensity. The dashed curves illustrate the effect of truncating the electron path length s in the integral, Eq. (2), whenever it exceeds the target thickness $s(E_0) \rightarrow \min[s(E_0), d]$. 10 keV to 1 MeV electrons have ranges from ~ 1 to ~ 700 μm in Cu.⁵³ Only a small fraction of the fastest electrons can escape the foil, resulting in quickly charging up the target and confining the rest of the electrons that are reflected back from surface sheath fields. Refluxing has previously been discussed in the context of proton generation, showing the importance of the recirculation of the MeV electrons on the electrostatic fields that accelerate protons to multi-MeV energies.³⁶ As expected, ignoring refluxing in the model shows disagreement with the experimental data by an order of magnitude or more. Physically, the solid curves correspond to the case where hot electrons are confined within the target due to reflection or “refluxing” from surface sheath fields until it is stopped, whereas the dashed curves correspond to the case where the electron and its energy are lost as soon as its path length equals the target thickness.

The solid curves can be made to agree quantitatively with the experimental data if a $\sim 10\%$ laser to hot-electron coupling efficiency is assumed. This is lower than the $\eta_{L \rightarrow e} \sim (20\% \text{ to } 40\%)$ usually quoted in the literature for these intensities, e.g., in Refs. 4–8 (upper solid curve). Conversion efficiencies were measured at the NOVA laser facility, yielding 5%–10% for 20 ps, 200 J, 2×10^{18} W/cm², 10%–15% for 5 ps, 300 J, 1×10^{19} W/cm², and up to 50% for 0.5 ps, 400 J, 3×10^{20} W/cm².^{6,8} There is a trend of increasing efficiency with laser intensity while our data would indicate a constant coupling efficiency. Possible explanations might be (1) differences in the details of the density profile. The NOVA experiments were performed with an intensity contrast of 5×10^3 – 5×10^4 while 10^5 – 10^7 is reported in these experiments. Hydrodynamic effects are probably not negligible at 20 ps pulse duration. (2) A coupling efficiency that increases with laser intensity might be compensated for thin foil targets (NOVA used several 100 μm thick layers) by a growing number of hot electrons leaving the target and making refluxing less efficient. The simple model that was used here and the relative large uncertainty of the experimental points allow only an estimate of the coupling efficiency, while more precise measurements require a careful CCD calibration and elaborate modeling, as it was done in Refs. 6 and 8.

V. SUMMARY AND CONCLUSIONS

For the first time, He_α and Ly_α lines in the K-shell emission of solid Cu targets irradiated with a 0.7 ps petawatt laser beam were observed at intensities $> 10^{20}$ W/cm². This is attributed to the formation of a ~ 2 to 3 keV near-solid-density hot plasma on the laser irradiation target side. A suppression of the ionic line emission is observed when the Cu targets are

coated with either a 1 μm thin layer of aluminum or with a 0.5 μm tantalum layer, indicating that the strongest heating is confined to a thin layer.

Measurements of the K-shell emission as a function of foil thickness between 30 μm and 1 μm for a constant laser intensity of $\sim 3 \times 10^{18} \text{ W/cm}^2$ and ~ 10 ps pulses show that the He_α emission varies by a factor of ~ 4 with a peak at 5 μm thickness, while the K_α yield stays about constant. A decreased K_α yield measured for targets thinner than 3 μm may be explained by a stronger heating of the small target volume and an increased hot-electron energy transfer into ions. Changing laser conditions especially affecting the surface layer could cause the variation of the He_α emission. The current data set is limited by its small sample size, and more shots are necessary to investigate this observation.

The K-shell emission of solid Cu foil targets was studied as a function of laser intensity between $2 \times 10^{18} \text{ W/cm}^2$ up to $3 \times 10^{20} \text{ W/cm}^2$ in low-area ($\sim 0.5 \times 0.5$ to $2 \times 2 \text{ mm}^2$) thin foils (~ 20 to $30 \mu\text{m}$) and 0.7-ps pulses. The yield of the ionic lines strongly increases with laser intensity such that, at the maximum intensity, the spectrum is dominated by the He_α emission. An approximately constant yield of $\sim 2 \times 10^{11}$ photons/J and $\sim 2 \times 10^{10}$ photons/J were measured for the K_α and K_β inner-shell emission, respectively, between intensities of $2 \times 10^{18} \text{ W/cm}^2$ and $1 \times 10^{20} \text{ W/cm}^2$. Above $1 \times 10^{20} \text{ W/cm}^2$, the inner-shell emission yield slightly drops. A comparison of the measured intensity scaling of the K_α yield with a model shows that refluxing of suprathermal electrons and their confinement in the target volume is crucial to explain these results. Calculations that ignore refluxing show a strongly decreasing K_α yield with laser intensity and disagree with the experimental data by more than an order of magnitude.

ACKNOWLEDGMENTS

This work was supported by the U.S. Department of Energy Office of Inertial Confinement Fusion under Cooperative Agreement No. DE-FC52-92SF19460, the University of Rochester, the New York State Energy Research and Development Authority, and the University of California Lawrence Livermore National Laboratory under Contract No. W-7405-Eng-48 UCRL-PRES213395. The support of the DOE does not constitute an endorsement by the DOE of the views expressed in this paper.

- ¹M. Tabak, J. Hammer, M. E. Glinsky, W. L. Kruer, S. C. Wilks, J. Woodworth, E. M. Campbell, M. D. Perry, and R. J. Mason, *Phys. Plasmas* **1**, 1626 (1994).
- ²O. L. Landen, D. R. Farley, S. G. Glendinning *et al.*, *Rev. Sci. Instrum.* **72**, 627 (2001).
- ³H.-S. Park, N. Izumi, M. H. Key, J. A. Koch, O. L. Landen, P. K. Patel, T. W. Phillips, and B. B. Zhang, *Rev. Sci. Instrum.* **75**, 4048 (2004).
- ⁴K. B. Wharton, S. P. Hatchett, S. C. Wilks *et al.*, *Phys. Rev. Lett.* **81**, 822 (1998).
- ⁵S. P. Hatchett, C. G. Brown, T. E. Cowan *et al.*, *Phys. Plasmas* **7**, 2076 (2000).
- ⁶K. Yasuike, M. H. Key, S. P. Hatchett, R. A. Snavely, and K. B. Wharton, *Rev. Sci. Instrum.* **72**, 1236 (2001).
- ⁷R. Kodama, K. Mima, K. A. Tanaka *et al.*, *Phys. Plasmas* **8**, 2268 (2001).
- ⁸M. H. Key, M. D. Cable, T. E. Cowan *et al.*, *Phys. Plasmas* **5**, 1966 (1998).
- ⁹P. A. Norreys, M. Santala, E. Clark *et al.*, *Phys. Plasmas* **6**, 2150 (1999).

- ¹⁰K. A. Tanaka, R. Kodama, H. Fujita *et al.*, *Phys. Plasmas* **7**, 2014 (2000).
- ¹¹J. A. Koch, M. H. Key, R. R. Freeman, S. P. Hatchett, R. W. Lee, D. Pennington, R. B. Stephens, and M. Tabak, *Phys. Rev. E* **65**, 016410 (2001).
- ¹²R. B. Stephens, R. A. Snavely, Y. Aglitskiy *et al.*, *Phys. Rev. E* **69**, 066414 (2004).
- ¹³S. C. Wilks, W. L. Kruer, M. Tabak, and A. B. Langdon, *Phys. Rev. Lett.* **69**, 1383 (1992).
- ¹⁴B. F. Lasinski, A. B. Langdon, S. P. Hatchett, M. H. Key, and M. Tabak, *Phys. Plasmas* **6**, 2041 (1999).
- ¹⁵L. Gremillet, G. Bonnaud, and F. Amiranoff, *Phys. Plasmas* **9**, 941 (2002).
- ¹⁶Y. Sentoku, K. Mima, P. Kaw, and K. Nishikawa, *Phys. Rev. Lett.* **90**, 155001 (2003).
- ¹⁷A. R. Bell and R. J. Kingham, *Phys. Rev. Lett.* **91**, 035003 (2003).
- ¹⁸A. J. Kemp, Y. Sentoku, T. Cowan, J. Fuchs, and H. Ruhl, *Phys. Plasmas* **11**, L69 (2004).
- ¹⁹A. R. Bell, J. R. Davies, S. Guerin, and H. Ruhl, *Plasma Phys. Controlled Fusion* **39**, 653 (1997).
- ²⁰T. Feurer, W. Theobald, R. Sauerbrey *et al.*, *Phys. Rev. E* **56**, 4608 (1997).
- ²¹R. Kodama, Y. Sentoku, Z. L. Chen *et al.*, *Nature (London)* **432**, 1005 (2004).
- ²²H. Chen, B. Soom, B. Yaakobi, S. Uchida, and D. D. Meyerhofer, *Phys. Rev. Lett.* **70**, 3431 (1993).
- ²³A. Rousse, P. Audebert, J. P. Geindre, F. Fallières, and J. C. Gauthier, *Phys. Rev. E* **50**, 2200 (1994).
- ²⁴D. C. Eder, G. Pretzler, E. Fill, K. Eidmann, and A. Saemann, *Appl. Phys. Lett.* **70**, 211 (2000).
- ²⁵H. R. Griem, *Spectral Line Broadening By Plasmas* (Academic, New York, 1974).
- ²⁶C. N. Danson, P. A. Brummitt, R. J. Clarke *et al.*, *Nucl. Fusion* **44**, S239 (2004).
- ²⁷C. N. Danson, J. Collier, D. Neely *et al.*, *J. Mod. Opt.* **45**, 1653 (1998).
- ²⁸P. K. Patel, M. H. Key, A. J. Mackinnon *et al.*, *Plasma Phys. Controlled Fusion* **47**, B833 (2005).
- ²⁹F. N. Beg, A. R. Bell, A. E. Dangor *et al.*, *Phys. Plasmas* **4**, 447 (1997).
- ³⁰C. Stoeckl, W. Theobald, T. C. Sangster, M. H. Key, P. Patel, B. B. Zhang, R. Clarke, S. Karsch, and P. Norreys, *Rev. Sci. Instrum.* **75**, 3705 (2004).
- ³¹M. Nishiuchi, K. Koyama, T. G. Tsuru, H. Awaki, H. Tomida, K. Hamaguchi, and H. Tsunemi, in *EUV, X-Ray, and Gamma-Ray Instrumentation for Astronomy IX*, edited by O. H. Siegmund and M. A. Gummin (SPIE, Bellingham, WA, 1998), Vol. 3445, p. 268.
- ³²D. H. Lumb and A. D. Holland, *Nucl. Instrum. Methods Phys. Res. A* **273**, 696 (1988).
- ³³H.-S. Park (private communication, 2005).
- ³⁴J. A. Bearden, *Rev. Mod. Phys.* **39**, 78 (1967).
- ³⁵R. L. Kelly, *J. Phys. Chem. Ref. Data* **16**, 651 (1987).
- ³⁶A. J. Mackinnon, Y. Sentoku, P. K. Patel, D. W. Price, S. Hatchett, M. H. Key, C. Andersen, R. Snavely, and R. R. Freeman, *Phys. Rev. Lett.* **88**, 215006 (2002).
- ³⁷H. Habara, K. L. Lancaster, S. Karsch *et al.*, *Phys. Rev. E* **70**, 046414 (2004).
- ³⁸D. E. Post, R. V. Jensen, C. B. Tarter, W. H. Grasberger, and W. A. Lokke, *At. Data Nucl. Data Tables* **20**, 397 (1977).
- ³⁹M. Green, *Solid-State Electron.* **3**, 314 (1961); M. Green and V. E. Cosslett, *Br. J. Appl. Phys., J. Phys. D* **1**, 425 (1968).
- ⁴⁰Prism Computational Sciences, Inc., Madison, WI, 53711.
- ⁴¹J. J. MacFarlane, I. E. Golovkin, P. R. Woodruff, D. R. Welch, B. V. Oliver, T. A. Mehlhorn, and R. B. Campbell, in *Inertial Fusion Sciences and Applications 2003*, edited by B. A. Hammel, D. D. Meyerhofer, J. Meyer-ter-Vehn, and H. Azechi (American Nuclear Society, La Grange Park, IL, 2004), p. 457.
- ⁴²H. K. Chung (private communication, 2005).
- ⁴³G. J. Pert, *J. Comput. Phys.* **43**, 111 (1981).
- ⁴⁴M. I. K. Santala, M. Zepf, I. Watts *et al.*, *Phys. Rev. Lett.* **84**, 1459 (2000).
- ⁴⁵M. Key (private communication, 2005).
- ⁴⁶S. Augst, D. Strickland, D. D. Meyerhofer, S. L. Chin, and J. H. Eberly, *Phys. Rev. Lett.* **63**, 2212 (1989).
- ⁴⁷L. Labate, C. A. Cecchetti, M. Galimberti, A. Giulietti, D. Giulietti, and L. A. Gizzi, *Phys. Plasmas* **12**, 083101 (2005).
- ⁴⁸R. P. J. Town, C. Chen, L. A. Cottrill, and *et al.*, *Nucl. Instrum. Methods Phys. Res. A* **544**, 61 (2005).
- ⁴⁹P. Gibbon and E. Förster, *Plasma Phys. Controlled Fusion* **38**, 769 (1996).

- ⁵⁰R. J. Mason, E. S. Dodd, and B. J. Albright, Phys. Rev. E **72**, 015401(R) (2005).
- ⁵¹G. Gregori, S. B. Hansen, R. Clarke, and *et al.*, Contrib. Plasma Phys. **45**, 284 (2005).
- ⁵²R. Snavely (private communication, 2005).
- ⁵³M. J. Berger, in *Methods in Computational Physics: Advances in Research and Applications*, Volume 1: Statistical Physics, edited by B. Alder, S. Fernbach, and M. Rotenberg (Academic, New York, 1963), p. 135.
- ⁵⁴H. Kolbenstvedt, J. Appl. Phys. **38**, 4785 (1967).
- ⁵⁵F. Ewald, H. Schwoerer, and R. Sauerbrey, Europhys. Lett. **60**, 710 (2002).
- ⁵⁶D. W. Forslund, J. M. Kindel, and K. Lee, Phys. Rev. Lett. **39**, 284 (1977).
- ⁵⁷G. Malka and J. L. Miquel, Phys. Rev. Lett. **77**, 75 (1996).
- ⁵⁸C. Hombourger, J. Phys. B **31**, 3693 (1998).